Computational Medical Physics Working Group Workshop II, Sep 30 – Oct 3, 2007
University of Florida (UF), Gainesville, Florida USA on CD-ROM, American Nuclear Society, LaGrange Park, IL (2007)

DEVELOPMENT OF HYBRID COMPUTATIONAL NEWBORN PHANTOM FOR DOSIMETRY CALCULATION: THE SKELETON

Deanna Hasenauer[*]
Department of Nuclear and Radiological Engineering
University of Florida
202 Nuclear Science Building
P.O. Box 118300
Gainesville, FL 32611-8300
UFDeanna@ufl.edu

Choonsik Lee
Department of Nuclear Engineering
University of Florida
202 Nuclear Science Building
P.O. Box 118300
Gainesville, FL 32611-8300
leecs@ufl.edu

Daniel L. Lodwick
Department of Nuclear Engineering
University of Florida
202 Nuclear Science Building
P.O. Box 118300
Gainesville, FL 32611-8300
acerpb@ufl.edu

Christopher J. Watchman
Department of Radiation Oncology
University of Arizona
P.O. Box 245081
1501 N. Campbell Ave.
Tucson, AZ 85721
watchman@email.arizona.edu

Dr. Wesley E. Bolch
Department of Nuclear Engineering
University of Florida
202 Nuclear Science Building
P.O. Box 118300
Gainesville, FL 32611-8300
wbolch@ufl.edu

[*] Funded under the Department of Energy Health Physics Fellowship Program

ABSTRACT

Computational phantoms have been used for decades in computing organ doses from occupational, medical, and accidental exposures from internal and external radiation sources. The evolution of computational phantoms began with mathematically based stylized phantoms, which allowed for organ repositioning and shape, but were anatomically unrealistic. Then, with the advent of image-based segmentation and more powerful computer processors, voxel-based phantoms utilizing 3D voxel matrices provided realistic anatomy, but at the expense of limited organ transformations. Current technology has led to the development of hybrid computational phantoms which combine the flexibility of organ redefinition in stylized phantoms and anatomical realism in voxel-based phantoms. The purpose of this study is to apply the Non-uniform rational B-spline (NURBS) advanced mathematical modeling tool to the University of Florida's voxel newborn phantom to replace the simple mathematical equations used in stylized phantoms, while preserving anatomical detail. ICRP Publications 70 and 89 report limited reference pediatric whole skeleton data based on uncertain assumptions. However in this study, newborn hybrid skeletal site-specific red bone marrow, yellow bone marrow, trabecular bone, cartilage, and cortical bone masses, volumes, densities, and elemental compositions were mathematically derived from image-based CT homogeneous bone segmentation, microCT data from newborn autopsy skeletal specimens acquired from UF Shands Hospital, along with some published data in ICRP, ICRU, and ORNL publications. Once established, this methodology can be replicated for the entire ICRP age series in an attempt to move away from masses tied to the stylized phantoms, and present additional skeletal data that is not found in ICRP or other literature resources.

The current 2003 Stabin and Siegel pediatric dosimetry models do not account for energy escape, cortical bone cross fire, or cellularity changes during transport. The models also use infinite two-dimensional chord-length distribution data from limited bone samples of a 1.7 year-old and a 9 year-old acquired at the University of Leeds, along with masses tied to the ORNL stylized phantoms. As skeletal size decreases, the effect of these limitations becomes more apparent. To address these issues, an EGSnrc computational Monte Carlo model was developed at the University of Florida. This Paired-Image Radiation Transport (PIRT) Model (Shah 2004) merges the actual CT three dimensional skeletal macrostructure with the imaged three-dimensional microstructure from skeletal specimens acquired via autopsy. Given the image-based methodology of obtaining skeletal data, the skeletal masses are tied to more realistic skeletal anatomy compared to the stylized masses. Preliminary results have shown between 5% and 35% overestimation at intermediate energies and between 35% and 150% overestimation at high energies in the current newborn model for some absorbed fraction results. Future studies will include a comprehensive assessment of internal electron and external photon skeletal dosimetry models, along with the development of corresponding age and skeletal site-dependent photon fluence-to-dose conversion factors, both which will take into account the non-homogeneity and finite size of bone tissue for the development of additional pediatric hybrid phantoms for the entire ICRP age series.

KEYWORDS: pediatric, skeleton, marrow, dosimetry, NURBS

1. INTRODUCTION

The human skeletal system consists of cortical bone, trabecular bone, bone marrow, periosteum, cartilage, and the blood vessels contained in those tissues. Among those tissues, bone marrow and bone surfaces are considered to be radio-sensitive and corresponding tissue weighting factors are assigned to those tissues by the International Commission on Radiological Protection (ICRP) [1]. To calculate radiation dose to those tissues, computational skeletal models have been developed and incorporated into Monte Carlo transport calculation codes.

Currently, two classes of computational skeletal models have been developed for dosimetry purposes: stylized (or mathematical) and voxel (or tomographic) models. Recently, it was shown that in order to correctly assess the skeletal-averaged specific absorbed fraction, each bone site-specific absorbed fraction must be associated with its corresponding bone site-specific tissue mass [2] [3] [4] [5] [6]. However, current reference masses are tied to the ORNL stylized dosimetry phantoms, which are represented by simplified geometric equations, and are defined for only gross tissue masses as a function of age. Developed by Snyder *et al*., the skeletal model of the Medical Internal Radiation Dose (MIRD) 5 phantom was the first stylized skeletal model representing that of the adult male, and consisted of six parts – leg bones, arm bones, pelvis, spine, skull, and ribs [7]. Even though the mathematical expressions have some extent of flexibility, due to both the limitations of mathematical equations and computation power at the development time, the stylized skeletal model was too simplified to accurately represent the complex details of the skeletal system. In addition, the whole skeleton was assumed to be homogenized to represent a mixture of skeletal components.

More advanced classes of skeletal models have been developed from medical images of real human subjects. The second generation of skeletal models describes the skeletal anatomy by using 3D voxel matrices which are segmented from computed tomography (CT) or magnetic resonance (MR) images. Even though some investigators developed MR-based skeletal models [8] [9] [10], CT images have provided better imaging accuracy of skeletal structures than MR images [11] [12] [13] [14]. Each bone site is semi-automatically segmented from CT images by utilizing the inherent contrast differentiation of bone from that of soft tissue. Investigators at the University of Florida have developed a series of pediatric skeletal models from CT images and included them with the series of whole body pediatric voxel phantoms for Monte Carlo calculations of red bone marrow and bone surface doses [15] [16]. It has been shown that the specific absorbed fractions to voxel-based or tomographic models may be greater or less than those to the MIRD-type of stylized models by factors up to 1000 for low energy gamma radiation [17].

Skeletal models for the pediatric population are different from those of adults in terms of topology and elemental composition. The newborn skeleton, specifically, is significantly different from those of more developed pediatric ages. The degree of cartilaginous ossification is much less than that of older pediatric ages. Subsequently, large amounts of the newborn skeleton are still not visible on CT images. Considering this point, unique elemental compositions and densities different from the older pediatric ages were assigned to the skeleton of newborn stylized phantom developed by Oak Ridge National Laboratory (ORNL) [18]. Even though the up-to-date voxel-based skeletal model of the UF voxel newborn phantom represents

more realistic skeletal structures than the ORNL stylized newborn phantom, it still has limitations as follows [16]. First of all, cartilage portions not shown in CT images were excluded or anatomically labeled incorrectly during segmentation of the skeleton. For example, cranial cartilage filling open fontanels or un-fused cranial sutures, specifically the anterior fontanel, were ignored and mistakenly considered as soft tissue. Also, inter-vertebral discs were incorrectly segmented as vertebral body structures. Moreover, the skeletal system of the UF voxel newborn phantom was fixed to that of the original newborn cadaver and has no flexibility to change its posture. This fixed skeletal model may not be applied to phantoms with varying postures. To address these limitations of the voxel-based skeletal model, this study was intended to develop a newborn hybrid skeletal model which simultaneously takes advantage of flexibility in the stylized skeletal model and anatomical realism of the voxel skeletal model.

In 1976 the University of Leeds published limited 2D chord-length distribution skeletal data on the trabecular bone and marrow cavity structures for a 1.7 and 9 year old child. Then, in an attempt to refine previous quantifications of the active marrow distribution in newborns to adulthood, Cristy estimated percentages of active marrow by bone site based on regional body sizes instead of individual bone sizes [19]. Later, ICRP Publication 70 [20] included a compilation of all skeletal data from newborn through adulthood from various sources dating back to 1926. However, the majority of pediatric skeletal microstructure information in ICRP 70 is based on the Leeds data of the 1.7-year and 9-year old. Finally, the ICRP Publication 89 document [21], included whole body (including skeleton) reference values for newborn through adult ages. The majority of the skeletal data reported in ICRP Publication 89 was already included in ICRP Publication 70. Given the lack of pediatric data available at the time of these publications, uncertain assumptions, such as 80% cortical bone and 20% trabecular bone for every age, and limited to no pediatric data on trabecular bone surface-to-volume ratios, or bone site-specific tissue masses have made it difficult to improve upon current pediatric skeletal models. Recently, skeletal sites such as the iliac crest, cervical spine, thoracic spine, lumbar spine, sternum, occipital bone, and ribs were acquired from newborn autopsies of 4-day and 5-day old cadavers at the University of Florida Shands Hospital and imaged via microCT scanning at SCANCO in Switzerland. In his 1981 article, Cristy made the claim that "*should age-dependent data on the volumes of individual bones as a percentage of total skeletal volume and the relative volumes of cortical and trabecular regions within each bone become available, a more accurate analysis of marrow distribution would be possible*." The newborn skeletal volumetric data from the CT images and microCT images in this study make this possible.

Computational phantoms have been used for decades in computing organ doses from occupational, accidental and medical exposures from both internal and external radiation sources. The evolution of computational phantoms began with mathematically based stylized phantoms, which allowed for organ repositioning and shape, but were anatomically unrealistic. Then, with the advent of image-based segmentation and more powerful computer processors, voxel-based phantoms utilizing 3D voxel matrices provided realistic anatomy, but at the expense of limited organ rescaling to match individual patient or subject anatomy. Current technology has led to the development of hybrid computational phantoms which combine the flexibility of organ redefinition in stylized phantoms with the anatomical realism of voxel-based phantoms. Applying the Non-uniform rational B-spline (NURBS) mathematical tool to segmented pediatric CT data will replace the simple mathematical equations used in stylized phantoms, while

preserving the anatomical accuracy provided by voxel-based models, for the development of the most anatomically detailed skeletal models possible. Current research at UF is focused on creating NURBS hybrid computational models for the entire ICRP age series (newborn, 1-year, 5-year, 10-year, and 15-year male and female subjects).

Existing dosimetry models of the adult skeleton used by the ICRP are based on limited microstructural information from a single 44 year-old male subject and use chord-length distributions that do not account for cortical bone cross-fire or particle escape into soft tissue at high electron energies. However, a 3D computational model, namely the Paired-Image Radiation Transport (PIRT) model, was developed at the University of Florida, and applied to refine the current ICRP Reference Man model [4] which explicitly accounts for both the trabecular microstructure (via microCT imaging) and the 3D shape and dimension of the adult skeletal site (via NURBS modeling). This EGSnrc Monte Carlo-based electron transport dosimetry model combines both the macrostructural and microstructural components of each imaged skeletal site in the Adult Man. Results showed that by not accounting for particle escape, the skeletal averaged absorbed fraction data are significantly greater at higher electron energies, causing an overestimation in the true dose [4]. Similarly, this model is being used to develop a voxel-based adult female model. Absorbed fraction results would have an even greater impact on children, where the overall skeletal size is significantly smaller than an adult. Unfortunately, very little efforts have been afforded to internal dosimetry models for the younger members of the general population. While internal photon doses to children are supported by the ORNL series of pediatric anatomic models, the detailed models of alpha and beta particle dose to the skeletal tissues are still relevant only to the adult male. Current pediatric skeletal models are also tied to stylized models instead of the more anatomically accurate phantoms and do not account for cellularity during transport (necessary at intermediate electron energies).

The present study was developed to specifically address the limitations of current pediatric skeletal models of Stabin and Siegel [22] model as noted above. These research efforts are intended to provide more anatomically accurate, comprehensive, and detailed age- and bone site-specific pediatric skeletal dosimetry models. This is important in medical patients for both radioiummotherapy (RIT) procedures where bone marrow is the dose-limiting tissue, and diagnostic procedures with external photon irradiation. Equal importance can also be found in radiation epidemiology studies, such as late effects in the Extended Techa River Cohort, involved with correlating biological effects of bone marrow dose to observed biological effects (e.g. cancers of both bone and bone marrow). The development of the NURBS pediatric skeletal dosimetry phantoms in this study will be conducted in parallel with the development of NURBS whole body dosimetry phantoms from additional research by the University of Florida's Pediatric Organ and Dosimetry (POD) research group. Once merged, the complete models (whole-body + detailed skeleton) will allow for a comprehensive dosimetry analysis involving multiple applications involving radiation exposures. The following section briefly summarizes the preliminary data acquired for the development of hybrid pediatric skeletal models by applying both the NURBS mathematical modeling tool to segmented in-vivo CT scans, and microCT data from selected bone sites collected at autopsy.

2. MATERIALS AND METHODS

2.1. Construction of the UF Hybrid Homogeneous Newborn Skeletal Model

To develop a hybrid skeletal model which has the flexibility of equation-based stylized skeletal models, two advanced mathematical tools were employed to replace conventional mathematical equations in this study: polygon mesh and non-uniform rational B-spline (NURBS) surfaces [23]. Polygon mesh is a simple solid made from the surfaces surrounded by the lines that connect vertices of the polygons called control points. NURBS surfaces are defined by weighted control points and knot vectors so that they precisely represent not only standard analytic shapes but free-form shapes such as the human anatomy. All skeletal sites of the hybrid skeletal model were described by polygon mesh except the ribs and costal cartilage, which were made using NURBS. NURBS surfaces can more effectively describe smooth surfaces and curvature of those bone sites with defect and continuity issues caused by low z-resolution. To provide anatomical realism to the hybrid skeletal model, the entire skeletal system from 485 CT slices of a 6-day-old female cadaver, which were also the source images for the UF voxel newborn phantom, was completely re-segmented. The voxel-based skeletal model of the UF voxel newborn phantom was not appropriate for this study because of the limitations briefly mentioned above. The cartilaginous regions of the skeletal system were not completely separated from ossified or compact bone. Therefore, fair comparisons could not be made between skeletal masses and reference values of ICRP Publication 89 [21]. The following is simply an overview of the exact methodologies employed in order to develop the hybrid skeletal model from CT images and investigate any significant differences compared to reference skeletal masses provided by ICRP Publication 89. Detailed methodologies and results of the UF hybrid whole body and skeletal phantoms are described in Lee *et al*. [24] and Hasenauer *et al*. (to be submitted to PMB), respectively.

2.1.1. Segmentation of homogeneous newborn skeleton and cartilage from CT data

To obtain the exact masses of cartilage and other skeletal tissues separately, they were re-segmented from original CT images of newborn female cadaver. Homogeneous skeleton except cartilage is defined as homogeneous bone including cortical bone, trabecular bone, miscellaneous skeletal tissues, inactive or yellow bone marrow (none in newborn) and active or red bone marrow. Original CT data were imported into *3D-DOCTOR* (Able Software Corp., Lexington, MA), 3D modeling and image processing software, to perform segmentation. In order to determine the correct lower bound of the threshold window, certain regions of cartilage were analyzed, such as the external nasal passages, ear lobes, and intervertebral discs. Once a threshold window was selected, the entire skeleton was reviewed for consistency of anatomy. After all bone sites were segmented, cartilage was segmented. Costal cartilage, cranial cartilage and intervertebral discs were manually segmented, while the 'other' (including external nose, ears, larynx, trachea, and extra-pulmonary bronchi) cartilage regions were not due to limited contrast resolution. Consequently, 'other' cartilage volumes were determined based on assumed relative fractions of total volumes for these regions.

2.1.2. Polygon mesh and NURBS modeling

Wavefront Object files generated by *3D-DOCTOR* were imported into *Rhinoceros* (McNeel North America, Seattle, WA) for polygon mesh and NURBS modeling. All of the bone sites were described by polygon mesh, but ribs were remodeled by using NURBS surfaces since some of the ribs were connected with each other due to the lower z-resolution than the in-between distance of each rib. Central contours and cross-sections of ribs were carefully obtained from original polygon mesh ribs, and pipe-shaped NURBS surfaces with a given cross-section were generated. NURBS surfaces for the ribs were generated from the body of the vertebrae to the costal cartilage extending from the sternum. The surfaces were cut down into ribs and costal cartilage by determining the position where each rib ended and costal cartilage regions began. After costal cartilage regions and ribs were separated, the mass of the NURBS rib model was calculated and matched that of the original ribs by adjusting the size of each rib cross-section.

2.1.3. Voxelization of homogeneous newborn skeleton

Currently, there is no Monte Carlo transport code to handle the polygon mesh or NURBS geometries. Therefore, polygon mesh and NURBS skeletal models cannot directly be incorporated into the Monte Carlo code for dosimetry calculations. The process relating polygon mesh and NURBS geometry to voxel medium, called voxelization process, is the most important technology utilized to develop hybrid skeletal models. The polygon mesh and NURBS skeletal models generated from *Rhinoceros* were voxelized into voxel-based skeletal model by using an in-house MATLAB code, *Voxelizer* [24]. A pre-processing step called triangulation was performed before voxelization for the NURBS surfaces. After NURBS surfaces are triangulated into polygons, vertices of each polygon are saved in ASCII Raw Triangles format. Another parameter called *voxel resolution* also caused volume differences during voxelization process. Fine *voxel resolution* results in accurate voxel models and higher voxel count. In the case of NURBS models, both parameters result in slight volume changes during the entire voxelization process. The only bone sites which were affected by *meshing tolerance* were the ribs and costal cartilage which were described by NURBS surfaces. All other bone sites were defined by polygon mesh so that only *voxel resolution* was considered as the parameter causing volume changes.

2.2. Construction of the UF Hybrid Heterogeneous Newborn Skeletal Model

Calculations of the newborn hybrid phantom's skeletal site-specific skeletal tissue masses, elemental compositions, and densities were performed using data from ICRP Publications 70 (ICRP 1995) and 89, ICRU Publication 44 (ICRU 1989), ICRU Publication 46 (ICRU 1992), volumetric microCT data from selected skeletal sites of 4 day and 5 day old newborn autopsy samples, and volumetric data from the NURBS newborn hybrid phantom skeletal model [24]. Given the slight volume difference between the NURBS and the reconstructed voxelized hybrid models (0.56 cm^3 for total skeleton cortical bone and spongiosa, 1.31 cm^3 for total cartilage, and 1.87 cm^3 for total skeleton), it should be noted that the skeletal volumes from the polygon mesh (NURBS for ribs and costal cartilage) hybrid model were used for all subsequent calculations. The rationale for this decision is based on the presumption that voxelizing the polygon mesh model at extremely fine resolutions would reduce the differences between the voxel and polygon mesh volumes to zero.

2.3. Electron Dosimetry Model for the Newborn Skeleton

Properly accounting for energy deposition within the trabecular microstructure requires information on the 3D geometry of the marrow cavities and bone trabeculae as a function of age and skeletal site. We have recently established an expedited IRB protocol at the UF Shands Hospital on the University of Florida campus to acquire selected skeletal specimens immediately following autopsy examination. Consequently, we have the unique opportunity to replace the interpolated Leeds chord-length distributions with directly measured microCT images of pediatric skeletal microstructure as needed for a full *PIRT* model calculation of skeletal dosimetry data. Subject will only be recruited if they did not have prolonged illness and bed rest, or did not die of illnesses known to alter normal skeletal microstructure. In late Spring of 2006, 4 day-old and 5 day-old infants were made available to us through the University of Florida Shands Hospital. Bone harvesting was conducted for the entire lumbar vertebrae series (L1 – L5), a portion of the thoracic series (T9 – T12), sternum, a small portion of the occipital bone, and two ribs of the 4 day-old. Five day-old samples of a majority of the spine (C3 – C7, T1 – T5, T10 – T12, L1 – L5), a single rib, and a portion of the iliac crest were collected. These samples were imaged via 30 micron resolution microCT at Scanco Medical AG in Switzerland and thus are available for complete *PIRT* model simulations. Similar images will thus be acquired across a range of pediatric ages using both the UF Shands Hospital IRB autopsy specimen collection protocol, and the Southeast Tissue Alliance (SETA) tissue recovery group.

Each bone site in the homogeneous newborn skeleton, created via NUBRS and polygon mesh modeling, was separated into cortical bone, spongiosa, and cartilage based on the tissue-specific volumetric derivations previously discussed. These bone sites were then individually voxelized using *Voxelizer* at resolutions between 50 μm^3 and 200 μm^3. These bones thus served as the macrostructure input into *PIRT*. Cross-sectional input data for *PIRT* were also generated by *PEGS4* using the derived skeletal site-specific elemental compositions and densities. Regions of interest were selected within the microCT-imaged microstructures for threshold processing of marrow and trabecular bone binary images. These macro- and micro-images were then coupled in the *PIRT* computational transport model for internal electron dosimetry of trabecular active marrow (TAM) or red bone marrow (RBM), trabecular inactive marrow (TIM) or yellow bone marrow (YBM), trabecular bone surface (TBS), trabecular bone volume (TBV), and cortical bone volume (CBV) sources to RBM, cartilage, and shallow active marrow (TAM_{50}) targets.

3. RESULTS AND DISCUSSION

3.1. Construction of the UF Hybrid Homogeneous Newborn Skeletal Model

Fig. 1 illustrates a comparison between the ORNL, segmented UF voxel and segmented UF hybrid-NURBS newborn skeletal models. To provide anatomical realism to the hybrid skeletal model, the entire skeletal system from 485 CT slices of a 6-day-old female cadaver (with approximate ICRP reference height and mass), which were also the source images for the UF voxel newborn phantom, was completely re-segmented separately into homogeneous bone (cortical bone plus spongiosa) and cartilage. Segmented object files generated by *3D-DOCTOR*, an advanced 3D modeling, image processing and measurement software program, were imported

into Rhinoceros®, Microsoft Windows software for polygon mesh and NURBS mathematical modeling. The skeleton and cartilage volumes were then adjusted uniformly until they matched the ICRP reference masses. The final total homogeneous skeleton NURBS and voxel masses were 239.4 g and 238.5 g, respectively. Therefore, the NURBS and voxel percent differences compared to the ICRP reference mass of 240.0 g were -0.26% and -0.61%, respectively. The total bone-associated NURBS and voxel cartilage masses were 127.8 g and 126.4 g, respectively, which is 0.4% (NURBS) and -0.7% (voxel) different compared to the ICRP reference mass of 127.3 g.

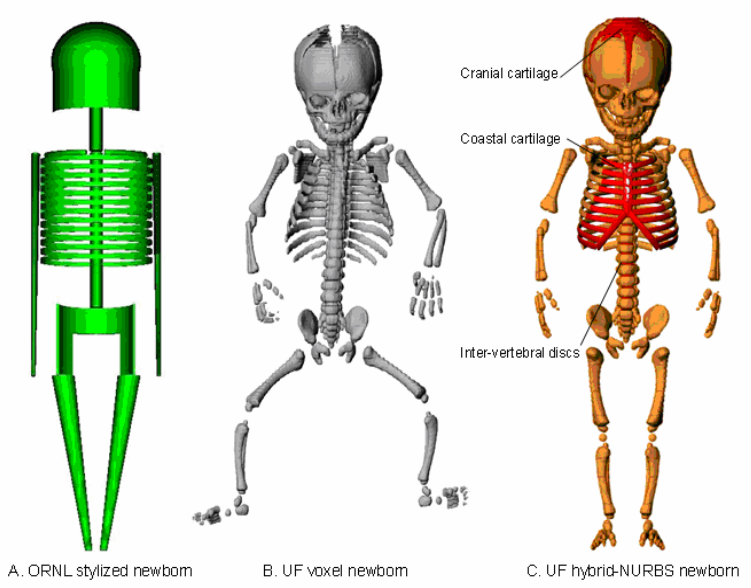

Figure 1. 3D renderings of skeleton models of (A) ORNL stylized, (B) UF voxel, and (C) UF hybrid-NURBS phantoms.

3.2. Derivation of Site-Specific Skeletal Tissues for the Newborn Skeletal Model

Once the UF hybrid-NURBS newborn homogeneous skeleton was constructed to match the ICRP newborn skeleton within a reasonable error tolerance, the skeletal tissues, namely red (active) bone marrow, yellow (inactive) bone marrow, miscellaneous skeletal tissues, trabecular bone, and cortical bone were distributed across individual bone sites of the newborn. These distributions were based on the volumetrically segmented newborn CT for total homogeneous bone site data, microCT skeletal data to get cortical bone, spongiosa and cartilage percentages, along with the threshold values utilized to generate marrow and bone volume fractions computed by an in-house image-processing code [25]. Fig. 2 (A) shows a single segmented transverse slice from the 4 day-old L3 vertebra, while Fig. 2 (B) illustrates the complete volumetrically segmented vertebra using the 3D rendering capabilities of *3D-DOCTOR*. The yellow, blue, and red segmented boundaries represent the cartilage, cortical bone, and spongiosa boundaries of skeletal tissue, respectively.

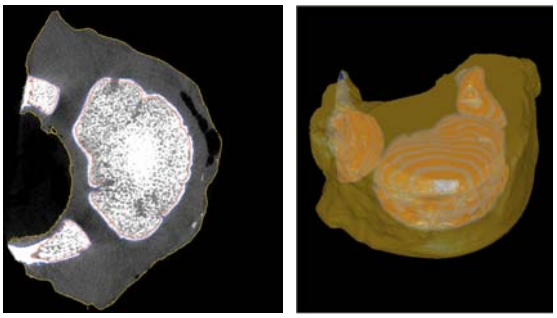

A. Transverse slice B. 3D-rendered

Figure 2. (A) Segmented transverse slice of 4 day-old L3 using 3D-Doctor and (B) 3D rendering of segmented 4 day-old L3 sing 3D-Doctor.

Single transverse slices from microCT images of the 4 day-old L3 vertebra and sternum, and 5 day-old iliac crest and rib samples are shown in Fig. 3 in the top row. White areas of the images are the trabecular spongiosa defining the marrow cavities (100% cellularity). The beginnings of the cortical bone cortex are also visible and show the centers of ossification for each bone site. The surrounding gray regions show the un-ossified tissues of cartilage in the newborn spine. Fig. 3 in the bottom row demonstrates the threshold sampled regions of interest selected from the corresponding newborn skeletal sites in the top row. The exact methodology conducted to distribute these bone tissues throughout the homogeneous skeleton will not be presented here, as all details are presented in Hasenauer *et al*. (to be submitted to *Phys. Med. Biol.*). However, overall results and comparisons with the current ICRP newborn skeletal distribution data will be shown.

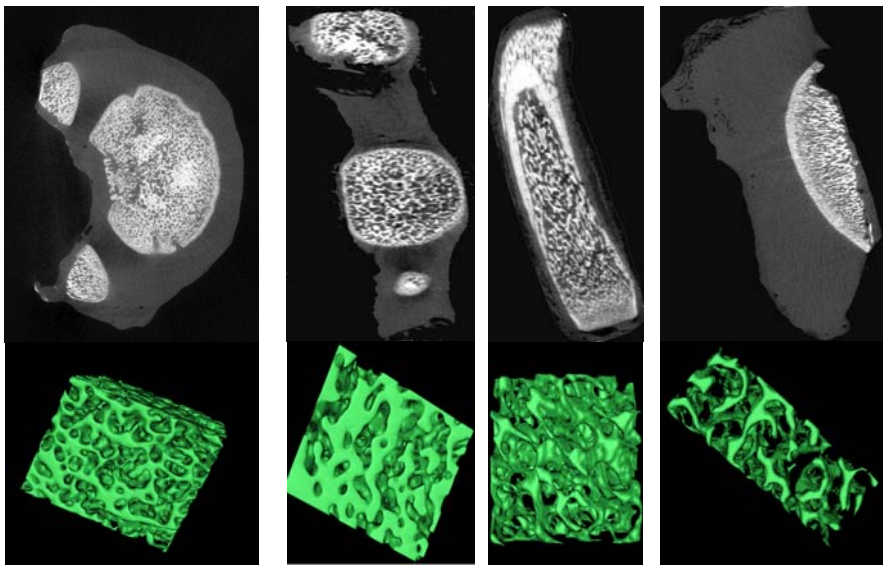

Figure 3. Transverse microCT slice of L3 (left), sternum (left-middle) excised from 4 day-old cadaver, and 4th rib (right-middle), iliac crest (right) excised from 5 day-old cadaver (above). MicroCT at 30 micron resolution for the corresponding bone sites (below).

Table I shows a comparison between the microCT-based newborn and ICRP newborn active marrow distributions. Most percentages were within 3% of the ICRP reference values. However, the ribs, thoracic vertebrae, and ankles and feet showed differences of -5.69%, 4.70%, and 4.70%, respectively. It should be noted that the ICRP active marrow distributions were calculated based on a body-region size corrected volumetric scaling of adult active marrow distributions [19]. Another important revision to the active marrow distributions is the separation of the extremities into proximal end, shaft, and distal end due to the structural and cellularity differences between the upper/lower shaft and the proximal and distal ends of the long bones. Current ICRP reference data on cortical and trabecular bone percentages as a function of total mineral bone for a specific bone are listed for the adult only. With the newborn image data provided by CT and microCT, it was possible to generate these percentages for the newborn. Table II shows the trabecular and cortical bone percentages calculated for the newborn compared with the adult values listed in ICRP 70. It should be noted that the extremity percentages for the newborn are based on the assumption that the rib serves as the best surrogate for the extremities. This assumption is based on the similar trabecular bone chord-distribution data between the rib and femur from the Leeds 1.7 year-old. Due to the unique chord-distributions of the cranium, the adult values were used as a default for the newborn.

Table I. Comparisons of active marrow percentages in the UF NURBS newborn and ICRP

Skeletal Site	NURBS/Polygon Mesh (%)	ICRP 89, Table 9.4 (%)	Difference (abs. %)
Cranium	28.61	27.00	-1.61
Mandible	3.21	2.50	-0.71
Cervical	2.09	3.40	1.31
Thoracic	3.60	8.30	4.70
Lumbar	2.40	2.40	0.00
Sternum	0.63	0.00	-0.63
Ribs	14.89	9.20	-5.69
Scapulae	2.91	2.70	-0.21
Clavicles	1.20	0.80	-0.40
Os coxae	6.26	9.20	2.94
Sacrum	0.96	0.10	-0.86
Humeri, Proximal	1.84	2.30	-0.42
Humeri, Upper Shaft	0.89		
Humeri, Lower Shaft	0.84	2.30	-0.23
Humeri, Distal	1.69		
Radii, Proximal	0.47		
Radii, Shaft	0.52	1.25	-0.46
Radii, Distal	0.73		
Ulnae, Proximal	0.88		
Ulnae, Shaft	0.65	1.25	-0.93
Ulnae, Distal	0.65		
Wrists and Hands	2.85	3.60	0.75
Femora, Proximal	3.00	3.70	-1.12
Femora, Upper Shaft	1.82		
Femora, Lower Shaft	2.84	3.70	-1.75
Femora, Distal	2.62		
Patellae	0.12	2.67	2.55
Tibiae, Proximal	2.10		
Tibiae, Shaft	1.99	2.67	-2.94
Tibiae, Distal	1.52		
Fibulae, Proximal	0.47		
Fibulae, Shaft	0.49	2.67	1.04
Fibulae, Distal	0.66		
Ankles and Feet	3.60	8.30	4.70
Total	100.00	100.00	0.00

Table II. Comparisons of cortical and trabecular bone percentages in the UF-hybrid NURBS newborn and ICRP adult model

	Newborn		Adult	
Skeletal Site	**Cortical**	**Trabecular**	**Cortical**	**Trabecular**
[1]Cranium	0.95	0.05	0.95	0.05
[2]Mandible	0.78	0.22	0.95	0.05
[3]Cervical	0.47	0.53	0.25	0.75
[3]Thoracic	0.47	0.53	0.25	0.75
[3]Lumbar	0.47	0.53	0.34	0.66
[4]Sternum	0.59	0.41	0.94	0.06
[2]Ribs	0.78	0.22	0.94	0.06
[5]Scapula	0.51	0.49	0.94	0.06
[5]Clavicles	0.51	0.49	0.94	0.06
[5]Os coxae	0.51	0.49	0.90	0.10
[3]Sacrum	0.47	0.53	0.75	0.25
[2]Humeri, upper half	0.78	0.22	0.90	0.10
[2]Humeri, lower half	0.78	0.22	0.90	0.10
[2]Radii	0.78	0.22	0.87	0.13
[2]Ulna	0.78	0.22	0.87	0.13
[2]Wrist and Hands	0.78	0.22	0.95	0.05
[2]Femora, upper half	0.78	0.22	0.77	0.23
[2]Femora, lower half	0.78	0.22	0.77	0.23
[2]Patella	0.78	0.22	0.77	0.23
[2]Tibia	0.78	0.22	0.83	0.17
[2]Fibula	0.78	0.22	0.89	0.11
[2]Ankles and Feet	0.78	0.22	0.65	0.35

[1]Adult value used as default

[2]100% 5 day old 4th rib

[3]100% 4 day old 3rd lumbar vertebra

[4]100% 4 day old sternum

[5]60:40 5 day old iliac crest to 4 day old 3rd lumbar vertebra

3.3. Electron Dosimetry Results for UF NURBS Newborn Skeleton

The dosimetry data provided can be used for radiation therapy applications (e.g. radioimmunotherapy), dose reconstruction applications (e.g Techa River dose reconstruction), and diagnostic procedures (e.g. CT and IVF procedures) to name a few. Shown in Fig. 4 are the newborn lumbar spine electron absorbed fraction data for a CBV source irradiating a TAM target. The two curves represent the assumed ICRP 30 value of 0.0 since the source does not equal the target and the computed *PIRT* values. At 150 keV, the currently assumed ICRP 30 absorbed fraction from cortical bone cross-fire is underestimated by about 40%, the highest percentage difference in this case. In the case of the Techa River dose reconstruction efforts, the average energy of Sr-90 is 200 keV, which by current models underestimates the true absorbed fraction by 40%. Fig. 5 is shown to illustrate the differences between using an infinite skeletal model, Voxel-Based Infinite Spongiosa Transport Model (*VBIST*) instead of allowing for electron escape (*PIRT*). A TBV source irradiating a TAM target in the newborn lumbar spine under *VBIST* assumptions can overestimate the true absorbed fraction results 1.36 times at 100 keV and up to 5.24 times at 10 MeV. Again, accounting for cortical bone cross-fire and electron escape has significant impacts in skeletal modeling. It should be noted that all absorbed fraction results were within 1% error at the 95% confidence interval.

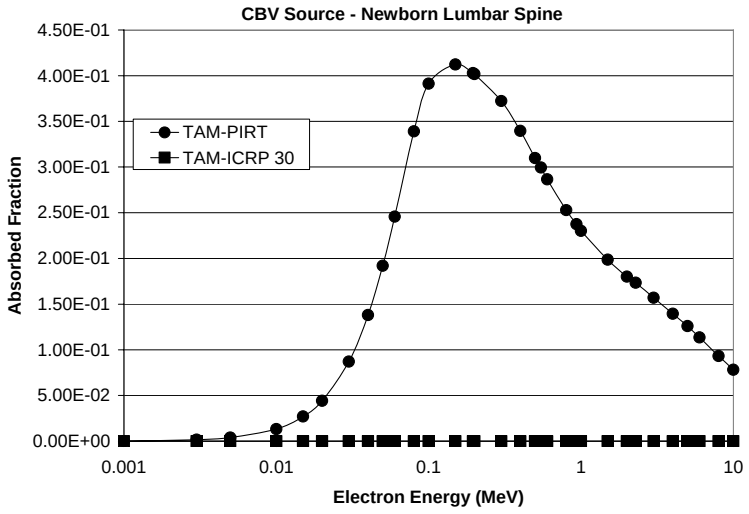

Figure 4. *PIRT* and ICRP comparison of absorbed fraction results for a CBV electron source irradiating a TAM target of the newborn lumbar spine.

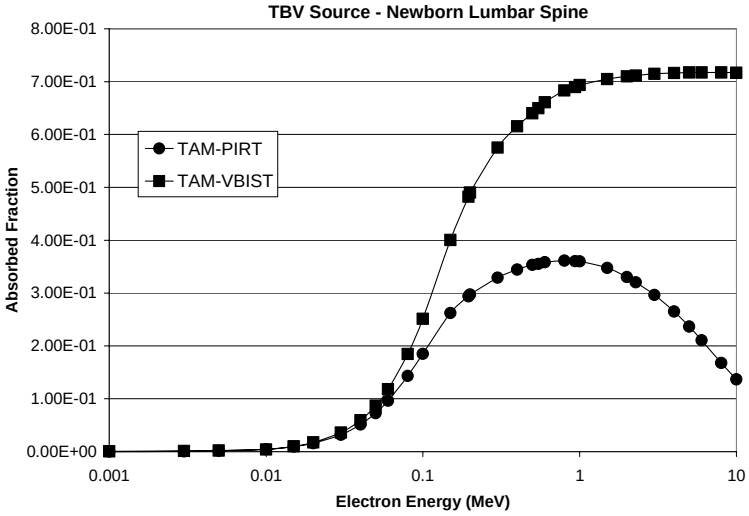

Figure 5. *PIRT* and *VBIST* comparison of absorbed fraction results for a TBV electron source irradiating a TAM target of the newborn lumbar spine.

4. CONCLUSIONS AND FUTURE WORK

NURBS modeling tools allow for the development of hybrid phantoms that combine the organ design and flexibility of stylized phantoms with the anatomical accuracy and detail of voxel-based phantoms. The development of the newborn NURBS/polygon mesh skeletal model was presented in this paper, along with methodologies to derive skeletal site-dependent tissue masses, densities, and elemental compositions based on the polygon mesh/NURBS volumes. Based on anatomically real volumetric CT data from a segmented newborn to get homogeneous bone volumes, and volumetric microCT data from newborn autopsy skeletal specimens, the calculated total skeletal tissue masses were in fairly good agreement with the ICRP reference newborn data.

The importance of this paper was the development and extension of the ICRP and ORNL reference total tissue data to skeletal site-specific tissue data, which will allow for an improved, anatomically realistic newborn skeletal model.

In this paper comparisons were made between infinite and non-infinite newborn skeletal models to show the importance of electron escape and cortical bone cross-fire, specifically at the newborn age. Future comparisons between the current 2003 Stabin and Siegel pediatric skeletal skeletal-averaged results will not only present the differences between chord-based and 3D image-based models, but more importantly the significance of reporting skeletal-site dependent data. This methodology will also be repeated for the entire ICRP age series. Ultimately, it is anticipated that the revised electron absorbed fraction data will have significant implications in the development of improved photon fluence-to-dose response function, which are currently based on infinite structure, and radionuclide S-values.

REFERENCES

1. ICRP. "Recommendations of the International Commission on Radiological Protection," *ICRP Publications 60*, (1990).
2. Shah A. P., Jokisch D., Watchman C., Rajon D., Patton P., and Bolch W. "Chord-Based Versus Voxel-Based Methods of Electron Transport in the Skeletal Tissues," *Med Phys*, **32**(10), pp. 3151-3159 (2005a).
3. Shah A. P., Rajon D., Jokisch D., Patton P., and Bolch W. "A Comparison of Skeletal Chord-Length Distributions in the Adult Male," *Health Phys*, **89**(3), pp. 199-215 (2005b).
4. Shah A. P., Rajon D., Patton P., Jokisch D., and Bolch W. "Accounting for Beta-Particle Energy Loss to Cortical Bone via Paired-Image Radiation Transport (*PIRT*)," *Med Phys*, **32**(5), pp. 1354-1366 (2005c).
5. Shah A. P., Patton P., Rajon D., and Bolch W. "Adipocyte Spatial Distributions in Bone Marrow: Implications for Skeletal Dosimetry Models," *J Nucl Med*, **44**(5), pp. 774-783 (2003).
6. Watchman C., Hasenauer D., Bolch W., "Derivation of Site-Specific Skeletal Masses within the Current ICRP Age Series", *Phys. Med. Biol.*, **52,** pp. 3133-3150 (2007).
7. Snyder W. S., Ford M. R., Warner G. G., and Fisher H. L. "Estimates of Absorbed Fractions for Monoenergetic Photon Sources Uniformly Distributed in Various Organs of a Heterogeneous Phantom," *MIRD Pamphlet No. 5*, (1969).
8. Jones D., "The Use of Voxel Phantoms in Organ Dose Calculations," *In: Workshop on Voxel Phantom Development*, Chilton, UK, National Radiological Protection Board, July 6-7, pp. 90-97 (1995).
9. Lee C., and Lee J. "Korean Adult Male Voxel Model KORMAN Segmented from Magnetic Resonance Images," *Med Phys*, **31**(5), pp. 1017-22 (2004).
10. Nagaoka T., Watanabe S., Sakurai K., Kunieda E., Taki M., and Yamanaka Y. "Development of Realistic High-Resolution Whole-Body Voxel Models of Japanese Adult Males and Females of Average Height and Weight, and Application of Models to Radio-Frequency Electromagnetic-Field Dosimetry," *Phys Med Biol*, **49**(1), pp. 1-15 (2004).
11. Fill U. A., Zankl M., Petoussi-Henss N., Siebert M., and Regulla D. "Adult Female Voxel Models of Different Stature and Photon Conversion Coefficients for Radiation Protection," *Health Phys*, **86**(3), pp. 253-272 (2004).
12. Lee C., Lee C., Park S. H., and Lee J. K. "Development of the Two Korean Adult Tomographic Computational Phantoms for Organ Dosimetry," *Med Phys*, **33**(2), pp. 380-390 (2006a).
13. Zankl M., and Wittmann A. "The Adult Male Voxel Model Golem Segmented from Whole-Body CT Patient Data," *Radiation and Environmental Biophysics*, **40**(2), pp. 153-162 (2001).
14. Zubal I. G., Harrell C. R., Smith E. O., Rattner Z., Gindi G., and Hoffer P. B., "Computerized Three-Dimensional Segmented Human Anatomy," *Med Phys*, **21**(2), pp. 299-302 (1994).
15. Lee C., Lee C., Williams J. L., and Bolch W. E., "Whole-Body Voxel Phantoms of Paediatric Patients - UF Series B," *Phys Med Biol*, **51**(17), pp. 4649-4661 (2006b).
16. Nipper J. C., Williams J. L., and Bolch W. E., "Creation of Two Tomographic Voxel Models of Pediatric Patients in the First Year of Life," *Phys Med Biol*, **47**(11), pp. 3143-3164 (2002).
17. Petoussi-Henss N., Zankl M., Fill U. and Regulla D. "The GSF Family of Voxel Phantoms," *Phys. Med. Biol,* **47,** 89-106 (2002).

18. Cristy M., and Eckerman K. F. "Specific Absorbed Fractions of Energy at Various Ages from Internal Photon Sources," *ORNL/TM-8381/Volumes I-VII*, (1987).
19. Cristy M., "Active Bone Marrow Distribution as a Function of Age in Humans," *Phys Med Biol*, **26**(3), pp. 389-400 (1981).
20. International Commission on Radiological Protection, *Basic Anatomical and Physiological Data for Use in Radiological Protection: The Skeleton*, *ICRP Publication 70*, Pergamon, Oxford, UK (1995).
21. International Commission on Radiological Protection, *Basic Anatomical and Physiological Data for Use in Radiological Protection: Reference Values*, *ICRP Publication 89*, Pergamon, New York, New York (2003).
22. Stabin M. G., and Siegel J. A., "Physical Models and Dose Factors for Use in Internal Dose Assessment," *Health Phys*, **85**(3), pp. 294-310 (2003).
23. Piegl L., "On NURBS: A Survey," *IEEE Computer Graphics and Applications*, **11**, pp. 55-71 (1991).
24. Lee C., Lodwick D., Hasenauer D., and Bolch W. E., "Development of Hybrid Computational Newborn Phantom for Dosimetry Calculation: Whole Body," *Phys Med Biol*, **52**, pp. 3309-3333 (2007).
25. Rajon D., Pichardo J., Brindle J., Kielar K., Jokisch D., Patton P., and Bolch W., "Image Segmentation of Trabecular Spongiosa by Visual Inspection of the Gradient Magnitude," *Phys Med Biol*, **51**(16), pp. 4447-67 (2006).